



Cite this: *J. Mater. Chem. A*, 2018, **6**, 8735

Encapsulating ionic liquids into POM-based MOFs to improve their conductivity for superior lithium storage†

Mi Zhang,^{‡,a} A-Man Zhang,^{‡,a} Xiao-Xiao Wang,^a Qing Huang,^a Xiaoshu Zhu,^b Xiao-Li Wang,^a Long-Zhang Dong,^{D,a} Shun-Li Li^{*a} and Ya-Qian Lan^{ID, *a}

Developing advanced anode materials with multi-electron reaction, adequate charge transport, and suppressed volume changes is highly desirable in lithium storage. Both polyoxometalates (POMs) and metal–organic frameworks (MOFs) are attractive candidates for anode materials because of strong multi-electron redox properties of the former and high surface areas and controllable porosities of the latter. However, the easy dissolution of POMs in an electrolyte and the intrinsically poor conductivity of MOFs result in inferior rate performance and cycling capacity. In this paper, we skillfully encapsulate ionic liquids (ILs) into polyoxometalate-based metal–organic frameworks (POMOFs) to fabricate a series of ILs-functionalized POMOF crystals (denoted as POMs-ILs@MOFs), in which POMs are immobilized in MOF cages to avoid the leaching of POMs. Also, an enhanced conductivity is obtained by the modification of ILs. One of the POMs-ILs@MOFs crystals, $\text{PMo}_{10}\text{V}_2\text{-ILs@MIL-100}$, when used as the anode material, shows superior cycling stability and high rate capability, which is proven to be the best amongst those of all the reported MOF, POM, and POMOF crystal materials. The outstanding performances are attributed to the hybrid behavior of a battery and a supercapacitor, which results from the synergistic effects of ILs, POMs, and MOFs. Most importantly, we not only discover a series of new anode materials but also propose a new strategy to improve the conductivity of MOFs and POMOFs, which will guide the development of other electrode materials based on MOFs and POMOFs for lithium storage.

Received 1st February 2018
Accepted 9th April 2018

DOI: 10.1039/c8ta01062e
rsc.li/materials-a

Introduction

Environmental problems and energy shortage are two serious issues related to human beings.¹ Currently, the search for new energy resources to replace traditional fossil energy has aroused great attention. Lithium-ion batteries (LIBs) have been vastly applied in consumer electronics and are regarded as one of the best candidates for next-generation power sources.^{2,3} Graphite is used as a commercial anode material for LIBs at present; however, it has a low theoretical capacity of about 372 mA h g^{-1} because of its tightly stacked layered structure.^{4,5} Therefore, great efforts have been made to develop other efficient anode materials. Among the potential anode materials, transition metal oxides,^{6–8} silicon,^{9,10} and amorphous phosphorus¹¹ have

received great attention. Nevertheless, the utilization of these lithium storage anode materials has been limited due to the slow lithium-ion (Li^+) diffusion process. In comparison, supercapacitors, which function based on the redox reactions of the pseudocapacitive active materials or the formation of electrical double-layer (EDL) capacitors, are also hampered in their application in electrochemical devices because of their low-energy density.^{12–14} Several alternative materials have been reported and there is great interest to fabricate new anode materials that combine the advantages of a battery and a supercapacitor for LIBs.

Polyoxometalates (POMs) as early transition metal anionic clusters have numerous applications in catalysis, magnetism, electronics, and energy conversion.¹⁵ Particularly, the high capability to accept a large number of electrons and the reversible multi-electron redox properties make POMs potential anode-active materials.^{16–18} However, when pristine POMs are used as anode materials, their anion is prone to dissolve in the electrolyte, which leads to an evident capacity degradation. To overcome this obstacle, POMs are usually linked to some proper substrates, such as metal–organic frameworks (MOFs), which possess high surface areas and controllable porosities and flexibility. This strategy has aroused enormous research

^aJiangsu Collaborative Innovation Centre of Biomedical Functional Materials, Jiangsu Key Laboratory of New Power Batteries, College of Chemistry and Materials Science, Nanjing Normal University, Nanjing 210023, P. R. China. E-mail: yqlan@njnu.edu.cn

^bCenter for Analysis and Testing, Nanjing Normal University, Nanjing 210023, P. R. China

† Electronic supplementary information (ESI) available. See DOI: [10.1039/c8ta01062e](https://doi.org/10.1039/c8ta01062e)

‡ Mi Zhang and A-Man Zhang contributed equally to this paper.

attention^{19–22} and has been applied in gas storage, separation, sensor, drug delivery, and energy storage.^{23–28} POMs can be encapsulated into MOFs to fabricate POMOF materials, which possess the properties of both POMs and MOFs and are attractive candidates for anode materials in lithium storage.²⁹ However, POMOFs have low cycling capacity and inferior rate performance due to their poor conductivity.³⁰ Recently, much effort has been devoted to design some conductive MOFs, which were used as the active electrode materials for EDL supercapacitors with outstanding electrochemical performances.^{31,32} Nevertheless, these conductive MOFs are all two-dimension materials, which are not suitable for the immobilization of POMs. To circumvent these difficulties, it is necessary to adopt other synthesis strategies to improve electronic conductivity of POMOFs as anode materials for LIBs. For example, our group has reported a novel nanocomposite based on POMOFs/RGO for LIBs, which has enhanced battery performance.³³ However, the synthesis of graphene oxide (GO) was a complex process, the homogeneity of this nanocomposite was out of control, and the POMOFs/RGO were not in the crystalline form. Thus, the method to prepare POMOF crystal materials having high conductivity and controllable homogeneity, which can directly determine electrochemical properties of the anode materials, is very crucial. In this work, we utilize ILs to tune or enhance the conductivity of POMOFs because of the high thermal and chemical stability, high ionic conductivity, and wide redox stability of ILs,³⁴ which make them great potential guest materials. If ILs and POMs are encapsulated into MOF cages simultaneously, the resulting anode materials are expected to have high capacity, good cycling stability, and rate behavior.

Herein, we synthesized PMo₁₀V₂-ILs@MIL-100 crystals using ferric chloride (Fe³⁺), benzene-1,3,5-tricarboxylic acid (BTC), 1-ethyl-3-methylimidazolium bromide (ILs), and H₅PMo₁₀V₂O₄₀ (PMo₁₀V₂) for the following reasons. (1) MIL-100 is synthesized from the precursors of Fe³⁺ and BTC, which have high thermal and chemical stability, high surface area, mesoporous cage structure (\approx 25 and 29 Å), and proper pentagonal and hexagonal windows (\approx 5.5 and 8.6 Å) (Fig. S1a†). MIL-100 can encapsulate many guest POMs and ILs due to the suitable size of the cavities and the mesoporous cage structure. (2) Keggin-type POMs such as PMo₁₀V₂ are widely used as anode materials owing to the proper size, high stability, water solubility, and reversible redox property which is stronger than that of PMo₁₂ because the V(v) atoms in the cluster can increase the redox potential of the first electron transfer reaction.³⁵ PMo₁₀V₂ can be confined into the mesoporous cage of MIL-100 owing to the fact that the size of PMo₁₀V₂ (\approx 10.47 Å) (Fig. S1b†) is bigger than the window size of the cage. PMo₁₀V₂ is inserted into the cages of MIL-100 to play the role of a bridge and then ILs are prone to disperse into the mesoporous cages of MIL-100 and react with PMo₁₀V₂ to form PMO₁₀V₂-ILs by an ion exchange procedure.³⁶ (3) ILs, especially the imidazolium ILs, possess high ionic conductivity and wide redox stability, which makes them attractive to improve the conductivity of POMOFs.³⁴ ILs in the POMOFs can not only enhance the contact between the electrolyte and the electrode but also improve the ionic and electronic conductivity of POMOFs and avoid the formation of thick solid-electrolyte

interphase (SEI) film.³⁷ Thus, the PMo₁₀V₂-ILs@MIL-100 crystals when used as an anode material for LIBs can achieve a high reversible capacity of 1248 mA h g^{−1} after 100 cycles at 0.1 A g^{−1}, an excellent rate capability of 480 mA h g^{−1} at 2.0 A g^{−1}, and a very long lifetime of 400 cycles with about 600 mA h g^{−1} retained at 1.0 A g^{−1}. It is worth to mention that the performances of PMo₁₀V₂-ILs@MIL-100 crystals are the best amongst all of the reported MOF-, POM- and POMOF-based crystal materials and comparable to the most excellent anode electrodes.

Besides, the lithium storage behavior of PMo₁₀V₂-ILs@MIL-100 and PMo₁₀V₂-ILs@HKUST-1 crystals is investigated by cyclic voltammetric (CV) measurement. It is observed that both samples show the hybrid behavior of a battery and a supercapacitor, and the larger mesoporous cages and the larger surface area of MIL-100 are beneficial to improve the contribution of capacitance. Although the synthesis of PMo₁₀V₂-ILs@MIL-100 crystals is complex and ionic liquids are not cheap, the most important purpose of this work is to provide a new strategy to improve the conductivity of MOFs and POMOFs and enhance their hybrid behavior, which will also guide the development of other electrode materials based on MOFs and POMOFs for lithium storage.

Experimental

Materials and synthetic procedures

Materials. All raw chemicals were obtained commercially and used without additional purification. The PMo₁₀V₂ precursor was synthesized according to a procedure described in the literature.³⁸

Synthesis of MIL-100(Fe) crystals. FeCl₃·6H₂O (1.62 g) and BTC (0.834 g) were dissolved in 30 mL of H₂O. The mixture was then transferred to a Teflon-lined autoclave, and heated to 130 °C, and kept at this temperature for 72 h. The product was filtered and washed with acetone.

Synthesis of PMo₁₀V₂@MIL-100 crystals. FeCl₃·6H₂O (0.945 g), BTC (0.68 g), and PMo₁₀V₂ (2.036 g) were dissolved in 25 mL of H₂O. The mixture was then heated to 130 °C and kept at this temperature for 72 h in a Teflon-lined autoclave. The product was filtered and washed with ethanol and ether.

Synthesis of PMo₁₀V₂@HKUST-1 crystals. Cu(OAc)₂·H₂O (0.2 g) and PMo₁₀V₂ (0.22 g) were dissolved in 10 mL of H₂O. BTC (0.14 g) was dissolved in 10 mL of alcohol, and this solution was added dropwise to the above mixture under continuous stirring. The precipitate was collected by centrifugation and washed with alcohol and deionized water.

Synthesis of PMo₁₀V₂-ILs@MIL-100 crystals and other control samples. An excess of ILs was dissolved in 25 mL of H₂O and then, PMo₁₀V₂@MIL-100 (2.0 g) was dispersed into the mixture. After that, the mixture was stirred at room temperature for 24 h. Finally, the product was collected by centrifugation and washed with diethyl ether. For comparison, PMo₁₂-ILs@MIL-100, PMo₁₀V₂-ILs@HKUST-1, and ILs@MIL-100 were synthesized through the same method, except that PMo₁₂@MIL-100, PMo₁₀V₂@HKUST-1, and MIL-100 were used respectively to replace PMo₁₀V₂@MIL-100.

Material characterization

The PXRD patterns were collected on a D/max 2500 VL/PC diffractometer (Japan) equipped with graphite monochromatized Cu K α radiation ($\lambda = 1.54060 \text{ \AA}$). The FTIR spectra were collected on a Nexus 670 spectrometer. TGA was carried out by using a DSC 800 analyzer from PerkinElmer under a N₂ flow with a heating rate of 10 °C min⁻¹ from room temperature to 700 °C. Nitrogen adsorption–desorption isotherms were evaluated at 77 K on a Micromeritics ASAP 2050 system, while the pore size distributions were calculated according to the Barrett–Joyner–Halenda (BJH) method. The TEM and HRTEM images were recorded on JEOL-2100F apparatus and JEOL JSM-6700 M scanning electron microscope, respectively. The EDS analyses were performed on a JSM-5160LV-Vantage typed energy spectrometer. XPS measurements were conducted on a scanning X-ray microprobe (PHI 5000 Verasa, ULAC-PHI, Inc.) using excitation energy of 1486.6 eV (Al K α) and the C 1s line at 284.8 eV as an energy reference.

Electrochemical characterization

To prepare a working electrode, active materials, carbon black, and poly (vinylidene fluoride) (PVDF) with a weight ratio of 7 : 2 : 1 were pasted on a piece of Cu foil. The loading of active materials for the electrode was around 1 mg. The half-coin cells were assembled in an argon-filled glove box with Li metal as a negative electrode, a solution of 1 M LiPF₆ in ethylene carbonate (EC) and dimethyl carbonate (DMC) (1 : 1 in volume) as the electrolyte, and a Celgard 2400 membrane as a separator. The galvanostatic charge/discharge measurement was conducted on a LAND CT2001A multichannel battery between 0.01 and 3.0 V. Electrochemical impedance spectra (EIS) measurements and CV were conducted on a CHI 660D electrochemical workstation (Shanghai, China). The conductivity of the sample pellets was measured with a two-probe method using Keithley 4200. The pellets of the samples were pressed at a pressure of ≈1 GPa.

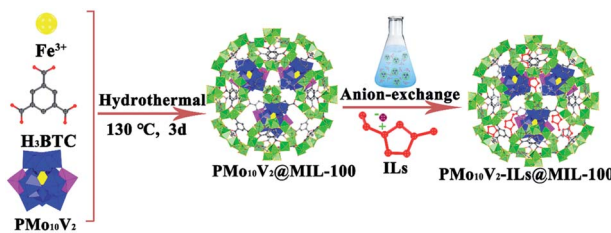
Results and discussion

The preparation process of PMo₁₀V₂-ILs@MIL-100 crystals is illustrated in Scheme 1. We first synthesized PMo₁₀V₂@MIL-100 using a facile hydrothermal method at 130 °C for 72 h using a simple mixture of Fe³⁺, BTC, and PMo₁₀V₂. ILs were then dispersed into the mesoporous cages of MIL-100 and reacted

with PMo₁₀V₂ to form PMo₁₀V₂-ILs by the ion exchange procedure. The crystal structure of PMo₁₀V₂-ILs@MIL-100 reveals that every trinuclear iron cluster is bridged by six BTC ligands to generate a 3D network (MIL-100) and PMo₁₀V₂-ILs are immobilized into the mesoporous cage of MIL-100 (Fig. S2a†). The MOFs and the POMs of the POMOFs may have great effects on the performances of LIBs. We utilized the same strategy to prepare other analogs of POM-ILs@MOFs and ILs@MOFs crystals, including PMo₁₂-ILs@MIL-100 (Fig. S2b†), PMo₁₀V₂-ILs@HKUST-1 (Fig. S2c†), and ILs@MIL-100 crystals, for comparison. The structure of PMo₁₂-ILs@MIL-100 crystals and ILs@MIL-100 are similar to that of PMo₁₀V₂-ILs@MIL-100 crystals, except that PMo₁₀V₂ is replaced by PMo₁₂ or without PMo₁₀V₂. However, compared with PMo₁₀V₂-ILs@MIL-100 crystals, PMo₁₀V₂-ILs@HKUST-1 crystals have the same internal material (PMo₁₀V₂-ILs) but different external structure (HKUST-1).

Powder X-ray diffraction (PXRD) was used to analyze the crystalline structure of the MIL-100, PMo₁₀V₂@MIL-100, and PMo₁₀V₂-ILs@MIL-100 crystals. The crystalline structure of MIL-100 and PMo₁₀V₂@MIL-100 is in agreement with the corresponding simulated patterns,³⁹ demonstrating that they have been synthesized successfully (Fig. 1a). The XRD patterns of PMo₁₀V₂-ILs@MIL-100 and PMo₁₀V₂@MIL-100 crystals are similar, which indicates that the diffusion of ILs into MIL-100 does not break the structure of POMOFs. The Fourier-transform infrared (FTIR) spectra of PMo₁₀V₂-ILs@MIL-100 crystals and other samples are shown in Fig. 1b. The bands at 1708 and 1366 cm⁻¹ in MIL-100, PMo₁₀V₂@MIL-100, and PMo₁₀V₂-ILs@MIL-100 crystals are attributed to the stretching vibrations of n(C=O) and n(C–O) originated from the aromatic groups. For the PMo₁₀V₂, PMo₁₀V₂@MIL-100 and PMo₁₀V₂-ILs@MIL-100 samples, four characteristic bands centered at 1057, 961, 865, and 776 cm⁻¹ are ascribed to P–O_c, Mo=O_t, Mo–O_b–Mo, and Mo–O_e–Mo stretching vibrations, respectively.^{40–42} Particularly, the bands at 3144 and 1582 cm⁻¹ in PMo₁₀V₂-ILs@MIL-100 are attributed to n(C–H) and n(C=N) stretching vibrations in the ILs, respectively, indicating that ILs have been successfully encapsulated into PMo₁₀V₂@MIL-100. The N₂ adsorption–desorption isotherms and pore size distributions of MIL-100, PMo₁₀V₂@MIL-100, and PMo₁₀V₂-ILs@MIL-100 crystals are shown in Fig. S3.† The surface area and the BJH pore size distribution also reflect the surface area and volume changes during the encapsulation process. The thermogravimetric analysis (TGA) analyses of MIL-100, PMo₁₀V₂@MIL-100, and PMo₁₀V₂-ILs@MIL-100 crystals are displayed in Fig. S4.†

The scanning electron microscopy (SEM) and the transmission electron microscopy (TEM) images reveal that all MIL-100 (Fig. S5a and b†), PMo₁₀V₂@MIL-100 (Fig. S5c and d†), and PMo₁₀V₂-ILs@MIL-100 (Fig. 1c and d) crystals have a uniform octahedron geometry with a size of approximately 300 nm. For the PMo₁₀V₂@MIL-100 and PMo₁₀V₂-ILs@MIL-100 crystals, compared with MIL-100, there is no obvious change after the encapsulation of PMo₁₀V₂ or the grafting of PMo₁₀V₂-ILs. Fig. 1e displays the corresponding energy dispersive X-ray spectroscopy (EDS) elemental mapping images of PMo₁₀V₂-ILs@MIL-100 crystals, which reveal that Fe, Mo, O, N, C, V, and P elements



Scheme 1 Schematic illustration of the synthetic process of PMo₁₀V₂-ILs@MIL-100 crystals.

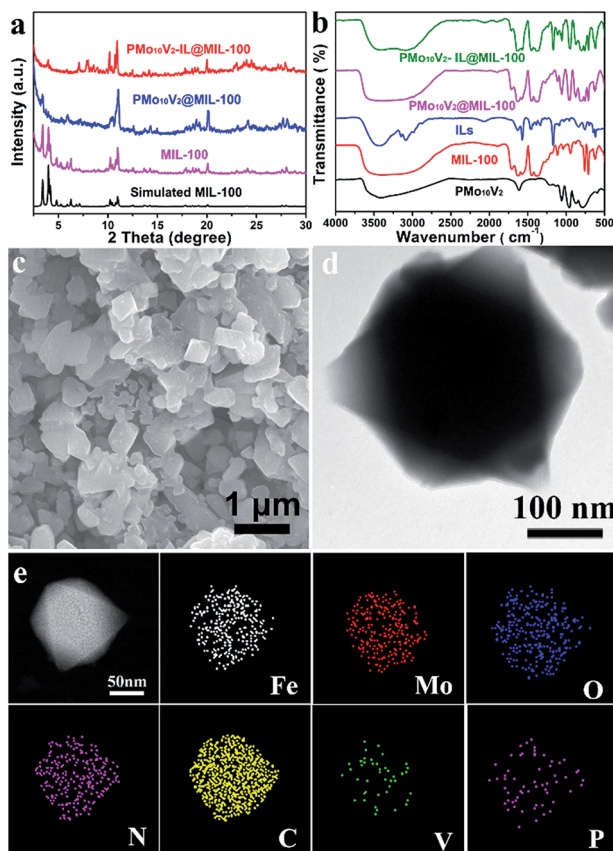


Fig. 1 (a) XRD patterns of simulated MIL-100, MIL-100, PMo₁₀V₂@-MIL-100, and PMo₁₀V₂-ILs@MIL-100 crystals. (b) FTIR spectra of PMo₁₀V₂, MIL-100, ILs, PMo₁₀V₂@MIL-100, and PMo₁₀V₂-ILs@MIL-100 crystals. (c) SEM image of PMo₁₀V₂-ILs@MIL-100 crystals. (d) TEM image of PMo₁₀V₂-ILs@MIL-100 crystals. (e) STEM image of PMo₁₀V₂-ILs@MIL-100 crystals and the corresponding mapping images of Fe, Mo, O, N, C, V, and P.

are distributed on the surface of PMo₁₀V₂-ILs@MIL-100 crystals uniformly.

The surface morphology and crystal structures of PMo₁₂-ILs@MIL-100 (Fig. S6a and b[†]) and PMo₁₀V₂-ILs@HKUST-1 (Fig. S6c and d[†]) are similar to those of PMo₁₀V₂-ILs@MIL-100, while PMo₁₀V₂-ILs@HKUST-1 has a bigger size compared with PMo₁₀V₂-ILs@MIL-100. The corresponding EDS elemental mapping images of PMo₁₂-ILs@MIL-100 and PMo₁₀V₂-ILs@HKUST-1 crystals are also shown in Fig. S7 and S8.[†]

X-ray photoelectron spectroscopy (XPS) is an efficient way to investigate the status of the surface atoms in crystals. Fig. S9[†] reveals the compositions and element valences of PMo₁₀V₂-ILs@MIL-100 crystals before and after discharge at 0.01 V. The XPS spectra of both samples indicate the existence of C, Fe, Mo, P, V, and O (Fig. S9a and f[†]). The peaks at 284.63, 285.8, and 288.6 eV correspond to the C-C/C=C, C-N, and HO-C=O, respectively (Fig. S9d[†]).¹⁶ The presence of a C-N group in the obtained crystals implies the existence of ILs in the PMo₁₀V₂@MIL-100 crystals. The O 1s signal can be deconvoluted to 531.23 eV (COOH), 532.15 eV (C=O), and 533.01 eV (C-O) (Fig. S9e[†]).¹⁶ Before the test, the Mo 3d core-level spectrum features two signals at binding energies of 232.5 and 235.85 eV,

corresponding to the Mo 3d_{3/2} and Mo 3d_{5/2} spin-orbit states of PMo₁₀V₂ (Fig. S9b[†]),¹⁷ respectively, indicating the presence of PMo₁₀V₂ in the crystals. After discharge, some of Mo⁶⁺ are reduced to Mo⁴⁺ as it can be seen by the appearance of Mo⁴⁺ peaks at the binding energy of 231.9 eV (Fig. S9g[†]).³³ In addition, as it can be seen in Fig. S9c,[†] the Fe 2p spectra have two different peaks of Fe 2p_{1/2} (725.4 eV) and Fe 2p_{3/2} (712.1 eV), demonstrating the existence of Fe³⁺.⁴³ After discharge, other two different peaks can be observed at 720.5 eV and 707.9 eV, corresponding to Fe⁰ state (Fig. S9h[†]).⁴⁴

The electrochemical properties of PMo₁₀V₂-ILs@MIL-100 crystals were first analyzed by CV over a voltage range of 0.01–3.0 V at a scan rate of 0.1 mV s⁻¹ (Fig. 2a). For the initial discharge cycle, a reduction peak at about 0.6 V is attributed to the formation of SEI films, which are protective layers formed on the electrode of LIBs as a result of electrolyte decomposition.⁴⁵ The peak is slightly shifted to the right (about 0.683 V) in the subsequent cycles after the SEI films are formed. After the first cycles, two obvious cathodic peaks at about 1.34 and 1.62 V and two anodic peaks at about 1.47 and 2.44 V are observed, which may be attributed to the reduction and oxidation of Mo and Fe, respectively (the XPS results in Fig. S9[†]).^{33,43} It is significant to note that the CV curves of the following cycles almost overlap, which indicates the excellent cycle stability of the PMo₁₀V₂-ILs@MIL-100 crystals.

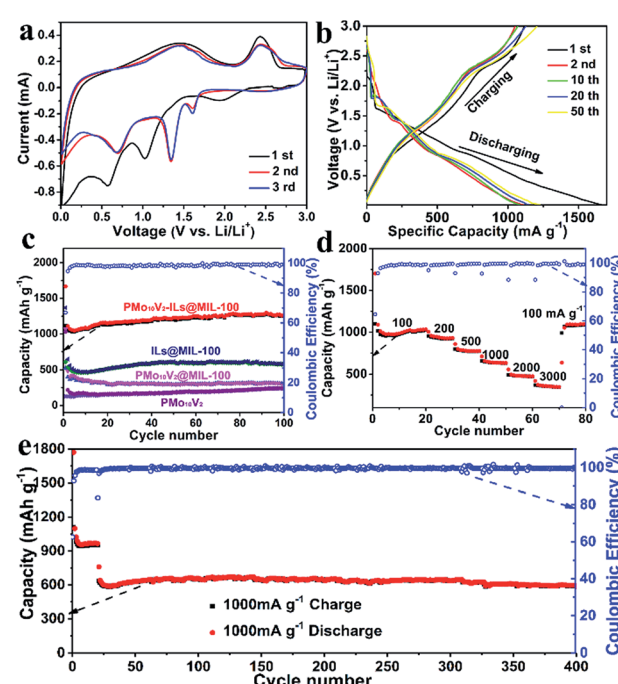


Fig. 2 (a) CV profiles of PMo₁₀V₂-ILs@MIL-100 crystals at a scan rate of 0.1 mV s⁻¹. (b) Galvanotactic charge-discharge curves of PMo₁₀V₂-ILs@MIL-100 crystals as anodes for LIBs for different cycles at 0.1 A g⁻¹. (c) Charge/discharge capacity and coulombic efficiency of PMo₁₀V₂, PMo₁₀V₂@MIL-100, ILs@MIL-100, and PMo₁₀V₂-ILs@MIL-100 crystals at 0.1 A g⁻¹. (d) Rate performance of PMo₁₀V₂-ILs@MIL-100 crystals from 0.1 A g⁻¹ to 3 A g⁻¹. (e) Cycling performance of PMo₁₀V₂-ILs@-MIL-100 crystals at 1.0 A g⁻¹ after a few cycles at 0.1 A g⁻¹.

The cycle performances of $\text{PMo}_{10}\text{V}_2\text{-ILs@MIL-100}$ crystals and other samples between 0.01 and 3 V at 0.1 A g^{-1} are displayed in Fig. 2c. $\text{PMo}_{10}\text{V}_2\text{-ILs@MIL-100}$ crystals display an initial discharge capacity of $1665.5 \text{ mA h g}^{-1}$ and a high reversible capacity of $1114.9 \text{ mA h g}^{-1}$ (Fig. 2b and c). By contrast, the control samples merely deliver initial discharge capacities of $1070.2 \text{ mA h g}^{-1}$ ($\text{PMo}_{10}\text{V}_2\text{@MIL-100}$), $1376.5 \text{ mA h g}^{-1}$ (ILs@MIL-100), $1031.4 \text{ mA h g}^{-1}$ ($\text{PMo}_{10}\text{V}_2$), and 1259 mA h g^{-1} (MIL-100) (Fig. S10†). The initial coulombic efficiency of $\text{PMo}_{10}\text{V}_2\text{-ILs@MIL-100}$ crystals is 66.94%, which is much higher than that of $\text{PMo}_{10}\text{V}_2\text{@MIL-100}$ (49.2%), ILs@MIL-100 (44.5%), $\text{PMo}_{10}\text{V}_2$ (12.56%), and MIL-100 (12.91%). In the subsequent cycles, $\text{PMo}_{10}\text{V}_2\text{-ILs@MIL-100}$ crystals maintain their capacity advantage over the control samples and a reversible capacity of $1258.5 \text{ mA h g}^{-1}$ is achieved after 100 cycles (Fig. 2c), which is more than twice that of ILs@MIL-100 ($581.4 \text{ mA h g}^{-1}$), three times larger than that of $\text{PMo}_{10}\text{V}_2\text{@MIL-100}$ ($310.5 \text{ mA h g}^{-1}$), and significantly larger than that of MIL-100 (75.7 mA h g^{-1}) and $\text{PMo}_{10}\text{V}_2$ ($242.3 \text{ mA h g}^{-1}$).

More importantly, the $\text{PMo}_{10}\text{V}_2\text{-ILs@MIL-100}$ crystals also display a superior rate performance (Fig. 2d). As the current density increases from 0.1 to 0.2, 0.5, 1, 2, and 3 A g^{-1} , the charge capacity of $\text{PMo}_{10}\text{V}_2\text{-ILs@MIL-100}$ crystals decrease slightly from 1032.8 to 929.2, 774.7, 633.6, 503.8, and $347.5 \text{ mA h g}^{-1}$, respectively. The capacity could reach $1104.6 \text{ mA h g}^{-1}$ when the current density is back to 0.1 A h g^{-1} , confirming the long-term stability of the $\text{PMo}_{10}\text{V}_2\text{-ILs@MIL-100}$ crystals. However, the performances of $\text{PMo}_{10}\text{V}_2\text{-ILs@MIL-100}$ crystals are poorer than those of $\text{PMo}_{10}\text{V}_2\text{-ILs@MIL-100}$ crystals (Fig. S11a and b†), which is ascribed to the fact that $\text{PMo}_{10}\text{V}_2$ has a stronger redox property because of the substitution of two V(v) atoms by Mo(vi) atoms. The electrochemical performances of the $\text{PMo}_{10}\text{V}_2\text{-ILs@HKUST-1}$ crystal electrodes were also investigated (Fig. S11a and b†). The $\text{PMo}_{10}\text{V}_2\text{-ILs@HKUST-1}$ electrode exhibits a similar stable cycling behavior as the $\text{PMo}_{10}\text{V}_2\text{-ILs@MIL-100}$ electrode, while the $\text{PMo}_{10}\text{V}_2\text{-ILs@HKUST-1}$ electrode shows much lower capacity during cycling, which is attributed to the fact that compared with HKUST-1, MIL-100 offers more space (Fig. S3a and b†) to hold ILs, which enhances conductivity, and the larger mesoporous cages (Fig. S12a and b†) improve the contribution of capacitance. In addition, the electrode prepared from $\text{PMo}_{10}\text{V}_2\text{-ILs@MIL-100}$ crystals maintains a capacity of about 600 mA h g^{-1} after 400 cycles at 1 A g^{-1} (Fig. 2e). $\text{PMo}_{10}\text{V}_2\text{-ILs@MIL-100}$ crystals exhibit excellent performances as compared to all MOF-, POM- and POMOF-based electrodes (Table S5†).

Electrochemical impedance spectra (EIS) of the $\text{PMo}_{10}\text{V}_2\text{@MIL-100}$ and $\text{PMo}_{10}\text{V}_2\text{-ILs@MIL-100}$ crystals after three cycles were also collected (Fig. S13a†). According to the fitting results, the $\text{PMo}_{10}\text{V}_2\text{-ILs@MIL-100}$ crystals show a smaller resistance than $\text{PMo}_{10}\text{V}_2\text{@MIL-100}$ (Table S1†) and the σ value can also be calculated from the slope (Fig. S13b†). At the third cycles, the ratio of $\sigma_{\text{PMo}_{10}\text{V}_2\text{-ILs@MIL-100}}/\sigma_{\text{PMo}_{10}\text{V}_2\text{@MIL-100}}$ is 0.3318, corresponding to $D_{\text{PMo}_{10}\text{V}_2\text{-ILs@MIL-100}}/D_{\text{PMo}_{10}\text{V}_2\text{@MIL-100}} \approx 9.08$, confirming that the Li^+ diffusion in $\text{PMo}_{10}\text{V}_2\text{-ILs@MIL-100}$ is faster than that in $\text{PMo}_{10}\text{V}_2\text{@MIL-100}$ (details can be seen in ESI†).

The conductivity of $\text{PMo}_{10}\text{V}_2\text{@MIL-100}$ and $\text{PMo}_{10}\text{V}_2\text{-ILs@MIL-100}$ powder pellets was also measured with a two-probe method used for a bulk powder. The bulk conductivity of $\text{PMo}_{10}\text{V}_2\text{-ILs@MIL-100}$ ($\sigma = 9.67 \times 10^{-6} \text{ S cm}^{-1}$) is 3.09×10^4 order of magnitude higher than that of $\text{PMo}_{10}\text{V}_2\text{@MIL-100}$ ($\sigma = 3.13 \times 10^{-10} \text{ S cm}^{-1}$) (Table S1†). All results indicate that the strong immobilization of ILs into $\text{PMo}_{10}\text{V}_2\text{@MIL-100}$ not only avails fast Li^+ and electronic transport and electrochemical activity during the Li^+ insertion/extraction, but also results in the favored interaction between the ILs and electrolyte, leading to a better electrochemical performance of the $\text{PMo}_{10}\text{V}_2\text{-ILs@MIL-100}$ crystals. To further investigate the electrochemical performance of $\text{PMo}_{10}\text{V}_2\text{-ILs@MIL-100}$ crystals, SEM analyses were performed to observe the morphology changes of the electrode after 100 cycles at 0.5 A g^{-1} . As shown in Fig. S14,† there is no significant change in the morphology, which indicates the stability of the electrode.

It is extremely surprising to obtain such high capacity for $\text{PMo}_{10}\text{V}_2\text{-ILs@MIL-100}$ crystals. In addition, compared with $\text{PMo}_{10}\text{V}_2\text{-ILs@HKUST-1}$ crystals, the practical capacity of $\text{PMo}_{10}\text{V}_2\text{-ILs@MIL-100}$ crystals highly exceeds the theoretical value (details can be seen in ESI†). The extra value may be derived from Li^+ intercalation into the mesoporous cages and the surface of $\text{PMo}_{10}\text{V}_2\text{-ILs@MIL-100}$ crystals. To further explain such high capacity, the capacitive effect of the battery system was studied according to the CV curves of the $\text{PMo}_{10}\text{V}_2\text{-ILs@MIL-100}$ crystals (Fig. 3a) and $\text{PMo}_{10}\text{V}_2\text{-ILs@HKUST-1}$ (Fig. S15a†) at different sweep rates from 0.1 to 10 mV s^{-1} . These results can be used to calculate the capacitance contribution in the electrochemical process on account of a power law $i = a \times v^b$,^{46–49} where i represents the current, v stands for the sweeping rate, and a and b are adjustable values. In general,

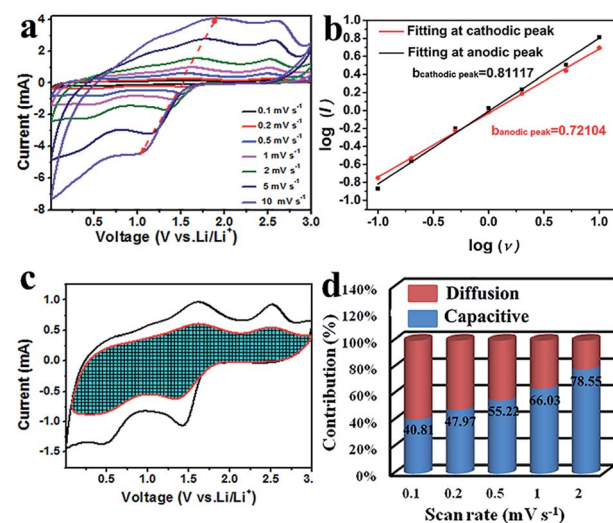


Fig. 3 (a) CV curves of $\text{PMo}_{10}\text{V}_2\text{-ILs@MIL-100}$ crystals at various scan rates from 0.1 to 10 mV s^{-1} . (b) b -value determination for cathodic and anodic peaks. (c) Capacitive-controlled charge storage contributions separated with cyclic voltammogram at 1 mV s^{-1} scan. (d) Normalized contribution ratio of capacitive (blue) and diffusion-limited (red) capacities at various scan rates.

a *b*-value of 0.5 indicates that the electrochemical reaction is mainly controlled by capacitance. A *b*-value of 1 means that it is regarded as a behavior which is controlled by the diffusion of Li⁺. When *b*-values are located between 0.5 and 1, both capacitance and the diffusion of Li⁺ contribute to the electrochemical process. As shown in Fig. 3b, the *b*-value is 0.811 for the cathodic peaks and 0.721 for the anodic one, which demonstrates a synergistic effect of capacitance and Li⁺ insertion/extraction. Furthermore, the PMo₁₀V₂-ILs@MIL-100 exhibits larger *b*-values in both cathodic and anodic scans in contrast to that of PMo₁₀V₂-ILs@HKUST-1 crystals (Fig. S15b†), confirming the improved rate performance and cycling capacity. The contributions of the capacitance and intercalation capacity can be further quantitatively calculated by the below equations:

$$i(v) = k_1 v + k_2 v^{0.5}$$

or

$$i(v)/v^{0.5} = k_1 v^{0.5} + k_2$$

By determining both k_1 and k_2 constants, we can analyze the fraction of the current originated from surface capacitance and Li⁺ diffusion at a given potential.^{33,50} As seen in Fig. 3c, the capacitive-controlled capacity contributes about 66.03% of the total Li⁺ storage for PMo₁₀V₂-ILs@MIL-100 crystals at 1 mV s⁻¹ (the blue shaded area of the Fig. 3c). As the scan rate rises from 0.1 to 2 mV s⁻¹, the effect of capacitive contribution gradually increases (Fig. 3d) and a maximum value of 78.55% at 2 mV s⁻¹ is obtained. However, as seen from Fig. S15c and d,† PMo₁₀V₂-ILs@HKUST-1 crystals show a lower capacitive contribution with a value of 51.05% at 1 mV s⁻¹ and 65.75% at 2 mV s⁻¹, which confirms that the larger mesoporous cages of MIL-100 compared with those of HKUST-1 can be beneficial in improving the contribution of capacitance.

As illustrated in Scheme S2,† the improved performances might be attributed to the synergistic effect of ILs, POMs, and MOFs, as following: first, the porous characteristics of MIL-100 can accommodate the volume expansion induced by the intercalation/deintercalation of Li⁺ and alleviate the stress. Second, the PMo₁₀V₂-ILs@MIL-100 crystals show a hybrid behavior of a battery and a supercapacitor. The battery behaviors of PMo₁₀V₂ are achieved by the redox of Mo⁶⁺, V⁵⁺, and Fe³⁺. At the same time, capacitive behavior also promotes the performance, which is ascribed to the mesoporous cages and the large surface area of MIL-100. Third, ILs in the MOFs can not only enhance the contact between electrolyte and electrode but also improve ionic and electronic conductivity due to the fast charge and Li⁺ transport. Accordingly, PMo₁₀V₂-ILs@MIL-100 crystal anode materials show excellent rate capability, remarkable cycling stability, and long-term cycle life.

Conclusions

In summary, we have successfully fabricated a series of POMs-ILs@MOFs crystals by encapsulating ILs within POMOFs. Owing to the strong redox properties of POMs and the high

porosities of MOFs, POMs-ILs@MOFs crystals show the hybrid behavior of a battery and a supercapacitor. In addition, ILs in the MOFs can not only provide a rapid path for Li⁺ transfer but also improve the electronic conductivity of POMOFs. Thus, when PMo₁₀V₂-ILs@MIL-100 crystals are used as anode materials for LIBs, they deliver a high capacity of 1248 mA h g⁻¹ at 0.1 A g⁻¹ after 100 cycles. The battery performances of PMo₁₀V₂-ILs@MIL-100 crystals, including capacity, cycling stability, and rate behavior, are significantly improved compared with those of the MIL-100, PMo₁₀V₂, PMo₁₀V₂@MIL-100, and ILs@MIL-100 crystals and are the best amongst all of the reported MOF-, POM- and POMOF-based crystal materials. The new strategy introduced herein to improve the conductivity of MOFs and POMOFs offers new prospects for the design of the next generation of high-performance and sustainable energy-storage devices based on different MOFs and POMOFs.

Conflicts of interest

There are no conflicts to declare.

Acknowledgements

This work was financially supported by NSFC (No. 21622104, 21471080 and 2170010097), the NSF of Jiangsu Province of China (No. SBK2017040708), the Natural Science Research of Jiangsu Higher Education Institutions of China (No. 17KJB150025), Priority Academic Program Development of Jiangsu Higher Education Institutions, and the Foundation of Jiangsu Collaborative Innovation Center of Biomedical Functional Materials.

Notes and references

- N. Armaroli and V. Balzani, *Angew. Chem., Int. Ed.*, 2007, **46**, 52–66.
- S. Xin, Y.-G. Guo and L.-J. Wan, *Acc. Chem. Res.*, 2012, **45**, 1759–1769.
- J. Chen and F. Cheng, *Acc. Chem. Res.*, 2009, **42**, 713–723.
- A. S. Arico, P. Bruce, B. Scrosati, J.-M. Tarascon and W. van Schalkwijk, *Nat. Mater.*, 2005, **4**, 366–377.
- L. Ji, Z. Lin, M. Alcoutlabi and X. Zhang, *Energy Environ. Sci.*, 2011, **4**, 2682–2699.
- S. H. Lee, S.-H. Yu, J. E. Lee, A. Jin, D. J. Lee, N. Lee, H. Jo, K. Shin, T.-Y. Ahn, Y.-W. Kim, H. Choe, Y.-E. Sung and T. Hyeon, *Nano Lett.*, 2013, **13**, 4249–4256.
- C. Li, T. Chen, W. Xu, X. Lou, L. Pan, Q. Chen and B. Hu, *J. Mater. Chem. A*, 2015, **3**, 5585–5591.
- K. Cao, L. Jiao, Y. Liu, H. Liu, Y. Wang and H. Yuan, *Adv. Funct. Mater.*, 2015, **25**, 1082–1089.
- F. Xia, S. B. Kim, H. Cheng, J. M. Lee, T. Song, Y. Huang, J. A. Rogers, U. Paik and W. I. Park, *Nano Lett.*, 2013, **13**, 3340–3346.
- H. Wu, G. Chan, J. W. Choi, I. Ryu, Y. Yao, M. T. McDowell, S. W. Lee, A. Jackson, Y. Yang, L. Hu and Y. Cui, *Nat. Nanotechnol.*, 2012, **7**, 310–315.

- 11 J. Qian, D. Qiao, X. Ai, Y. Cao and H. Yang, *Chem. Commun.*, 2012, **48**, 8931–8933.
- 12 K. S. Ryu, K. M. Kim, N.-G. Park, Y. J. Park and S. H. Chang, *J. Power Sources*, 2002, **103**, 305–309.
- 13 S. W. Lee, N. Yabuuchi, B. M. Gallant, S. Chen, B.-S. Kim, P. T. Hammond and Y. Shao-Horn, *Nat. Nanotechnol.*, 2010, **5**, 531–537.
- 14 X. Zhang, W. Shi, J. Zhu, D. J. Kharistal, W. Zhao, B. S. Lalia, H. H. Hng and Q. Yan, *ACS Nano*, 2011, **5**, 2013–2019.
- 15 Y. Ji, L. Huang, J. Hu, C. Streb and Y.-F. Song, *Energy Environ. Sci.*, 2015, **8**, 776–789.
- 16 J. Hu, H. Diao, W. Luo and Y.-F. Song, *Chem.–Eur. J.*, 2017, **23**, 8729–8735.
- 17 J. Xie, Y. Zhang, Y. Han and C. Li, *ACS Nano*, 2016, **10**, 5304–5313.
- 18 D. Ma, L. Liang, W. Chen, H. Liu and Y.-F. Song, *Adv. Funct. Mater.*, 2013, **23**, 6100–6105.
- 19 J. L. C. Rowsell and O. M. Yaghi, *Microporous Mesoporous Mater.*, 2004, **73**, 3–14.
- 20 A. Shigematsu, T. Yamada and H. Kitagawa, *J. Am. Chem. Soc.*, 2011, **133**, 2034–2036.
- 21 M. Sadakiyo, H. Okawa, A. Shigematsu, M. Ohba, T. Yamada and H. Kitagawa, *J. Am. Chem. Soc.*, 2012, **134**, 5472–5475.
- 22 S. Bureekaew, S. Horike, M. Higuchi, M. Mizuno, T. Kawamura, D. Tanaka, N. Yanai and S. Kitagawa, *Nat. Mater.*, 2009, **8**, 831–836.
- 23 A. Morozan and F. Jaouen, *Energy Environ. Sci.*, 2012, **5**, 9269–9290.
- 24 O. Shekhah, J. Liu, R. A. Fischer and C. Woll, *Chem. Soc. Rev.*, 2011, **40**, 1081–1106.
- 25 X. Li, F. Cheng, S. Zhang and J. Chen, *J. Power Sources*, 2006, **160**, 542–547.
- 26 R. Senthil Kumar, C. Nithya, S. Gopukumar and M. Anbu Kulandainathan, *Energy Technol.*, 2014, **2**, 921–927.
- 27 T. An, Y. Wang, J. Tang, Y. Wang, L. Zhang and G. Zheng, *J. Colloid Interface Sci.*, 2015, **445**, 320–325.
- 28 L. Bai, B. Tu, Y. Qi, Q. Gao, D. Liu, Z. Liu, L. Zhao, Q. Li and Y. Zhao, *Chem. Commun.*, 2016, **52**, 3003–3006.
- 29 D.-Y. Du, J.-S. Qin, S.-L. Li, Z.-M. Su and Y.-Q. Lan, *Chem. Soc. Rev.*, 2014, **43**, 4615–4632.
- 30 Y. Yue, Y. Li, Z. Bi, G. M. Veith, C. A. Bridges, B. Guo, J. Chen, D. R. Mullins, S. P. Surwade, S. M. Mahurin, H. Liu, M. P. Paranthaman and S. Dai, *J. Mater. Chem. A*, 2015, **3**, 22989–22995.
- 31 W.-H. Li, K. Ding, H.-R. Tian, M.-S. Yao, B. Nath, W.-H. Deng, Y. Wang and G. Xu, *Adv. Funct. Mater.*, 2017, **27**, 1702067.
- 32 D. Sheberla, J. C. Bachman, J. S. Elias, C.-J. Sun, Y. Shao-Horn and M. Dinca, *Nat. Mater.*, 2017, **16**, 220–224.
- 33 T. Wei, M. Zhang, P. Wu, Y.-J. Tang, S.-L. Li, F.-C. Shen, X.-L. Wang, X.-P. Zhou and Y.-Q. Lan, *Nano Energy*, 2017, **34**, 205–214.
- 34 S. S. Moganty, N. Jayaprakash, J. L. Nugent, J. Shen and L. A. Archer, *Angew. Chem., Int. Ed.*, 2010, **122**, 9344–9347.
- 35 M. Sadakane and E. Steckhan, *Chem. Rev.*, 1998, **98**, 219–238.
- 36 H. Wan, C. Chen, Z. Wu, Y. Que, Y. Feng, W. Wang, L. Wang, G. Guan and X. Liu, *ChemCatChem*, 2015, **7**, 441–449.
- 37 X. Qi, K.-Y. Pu, H. Li, X. Zhou, S. Wu, Q.-L. Fan, B. Liu, F. Boey, W. Huang and H. Zhang, *Angew. Chem., Int. Ed.*, 2010, **49**, 9426–9429.
- 38 G. A. Tsigdinos and C. J. Hallada, *Inorg. Chem.*, 1968, **7**, 437–441.
- 39 R. Canioni, C. Roch-Marchal, F. Sécheresse, P. Horcajada, C. Serre, M. Hardi-Dan, G. Férey, J.-M. Grenèche, F. Lefebvre, J.-S. Chang, Y.-K. Hwang, O. Lebedev, S. Turner and G. Van Tendeloo, *J. Mater. Chem.*, 2011, **21**, 1226–1233.
- 40 D. Zhou and B.-H. Han, *Adv. Funct. Mater.*, 2010, **20**, 2717–2722.
- 41 C. Rocchiccioli-Deltcheff, M. Fournier, R. Franck and R. Thouvenot, *Inorg. Chem.*, 1983, **22**, 207–216.
- 42 Z. Cui, C. X. Guo, W. Yuan and C. M. Li, *Phys. Chem. Chem. Phys.*, 2012, **14**, 12823–12828.
- 43 C. Zhang, W. Hu, H. Jiang, J.-K. Chang, M. Zheng, Q.-H. Wu and Q. Dong, *Electrochim. Acta*, 2017, **246**, 528–535.
- 44 M. C. Biesinger, B. P. Payne, A. P. Grosvenor, L. W. M. Lau, A. R. Gerson and R. S. C. Smart, *Appl. Surf. Sci.*, 2011, **257**, 2717–2730.
- 45 M. V. Reddy, G. V. Subba Rao and B. V. R. Chowdari, *Chem. Rev.*, 2013, **113**, 5364–5457.
- 46 J. Wang, H. Tang, L. Zhang, H. Ren, R. Yu, Q. Jin, J. Qi, D. Mao, M. Yang, Y. Wang, P. Liu, Y. Zhang, Y. Wen, L. Gu, G. Ma, Z. Su, Z. Tang, H. Zhao and D. Wang, *Nat. Energy*, 2016, **1**, 16072.
- 47 T. Yuan, Y. Jiang, W. Sun, B. Xiang, Y. Li, M. Yan, B. Xu and S. Dou, *Adv. Funct. Mater.*, 2016, **26**, 2198–2206.
- 48 P. Simon, Y. Gogotsi and B. Dunn, *Science*, 2014, **343**, 1210–1211.
- 49 V. Augustyn, P. Simon and B. Dunn, *Energy Environ. Sci.*, 2014, **7**, 1597–1614.
- 50 M. Zhang, T. Wei, A. M. Zhang, S.-L. Li, F.-C. Shen, L.-Z. Dong, D.-S. Li and Y.-Q. Lan, *ACS Omega*, 2017, **2**, 5684–5690.